Effect of Two Bogie Cavity Configurations on the Underbody Flow and Near Wake Structures of a High-Speed Train

G. Xu [1,2], H. Li[1], J. Zhang [2,3,4†] and X. Liang [2,3,4]

[1] *CRRC Qingdao Sifang Co., Ltd., Qingdao,Shandong, 266111, China*
[2] *Key Laboratory of Traffic Safety on Track of Ministry of Education, School of Traffic & Transportation Engineering, Central South University, Changsha 410075, China*
[3] *Joint International Research Laboratory of Key Technology for Rail Traffic Safety, Central South University, Changsha 410075, China*
[4] *National & Local Joint Engineering Research Center of Safety Technology for Rail Vehicle, Changsha 410075, China*

†*Corresponding Author Email: jie_csu@csu.edu.cn*

ABSTRACT

A time-dependent simulation method, DES (detached eddy simulation), combined with Realizable *k-ε* turbulence model, has been adopted to study the underbody flow and near wake structures of a high-speed train with two bogie cavity configurations laid on the stationary ground. The numerical data, including time-averaged aerodynamic drag forces and pressure coefficients, were compared with experimental results from previous wind tunnel tests. A detail comparison of the instantaneous flow structures, mean velocity vector contours, velocity and pressure profiles under the train bottom in the symmetry plane and velocity contours overlaid with streamlines in the wake has been conducted in the two configurations. Also the aerodynamic drag coefficients for the two cases are discussed herein. The two cases show that the bogie cavity configurations contribute to the differences of velocity and pressure distributions in each bogie region, as well as the complex vortex structures around the bogie regions. Compared to the inclined bogie cavity configuration, the train with straight plates experiences a lower drag force by 2.8% for a three-car model in the stationary ground. Thus, an effective simplification criterion for the train model will contribute to an accurate prediction of forces of trains in simulations.

NOMENCLATURE

C_p	pressure coefficient	u	time-averaged streamwise velocity
C_d	drag force coefficient	U	velocity
C_t	non-dimensional time	U_{inf}	inlet velocity
F_d	drag force	W	train width
H	train height		
L	train length	α	angle of front end
Q	second invariant	β	angle of rear end
S	reference area	k	turbulence kinetic energy
t	computation time in the simulation	ρ	air density
p	static pressure	ε	turbulence dissipation rate
p_{ref}	reference pressure		
q	dynamic pressure		

1. INTRODUCTION

In past decades, more and more new high-speed railway lines in excess of 250 km/h have been constructed around the world, in particular in China where the maximum of train speed is even up to 350 km/h. Some problems at the low train speed, such as aerodynamic drag, crosswind stability,

tunnel effect, aerodynamic noise, ground effect and slipstream can be ignored, have become extremely significant in railway operation. Thus, to enhance the operational safety of the train, improve the passenger's comfort and achieve energy saving and environmental protection requirements, many countries with high developed railway networks have conducted lots of research on the train aerodynamics. The investigation of underneath configurations on the bottom flow and near wake structures of a high-speed train has become one of the most interesting issues.

Mancini *et al.* (2001) carried out series of reduced- and full-scale tests to study how the bogie fairings could influence the total aerodynamic drag force of a new ETR 500 high-speed train. They found that the optimised fairings decrease the drag by up to 20% in a reduced scale test, while approximately 10 % in the full-scale test. Zheng *et al.* (2011) studied the effect of train's bottom shape on the aerodynamic drag of a high-speed train at a speed of 400 km/h, and found the train bottom shape can influence the drag distribution on the entire train, especially on the bottom. Niu *et al.* (2017) conducted simulations using improved delayed detached eddy simulation (IDDES) to understand the obstacle deflectors' effect on the aerodynamic forces of high-speed trains at 0° and 15° yaw angles. They also showed the underneath configurations cause the change of flow structures underneath the train head and in the wake. Zhang *et al.* (2018a) investigated 4 bogie cavity's angles on the aerodynamic drag force of the high-speed train. They further confirmed that the variations of bogie cavity's angles affect flow structures in the bogie regions and the near wake. Gao *et al.* (2018) performed Reynolds-averaged Navier-Stokes (RANS) simulations to understand the contribution of bogie positions to the drag force and the near wake structure of the high-speed train, and about 6% drag reduction is achieved. Thus, according to the previous research, more work on the bogie regions can be conducted.

To authors' knowledge, a train model used in simulations needs to be simplified to an extent. According to CEN Standards, there is no specification to points out which level can be accepted. Therefore, researchers in the field of train aerodynamics generally follow the CEN Standards, but also make some extra simplification. As a result, the bogie cavity may be assigned straight or inclined walls at the ends. In the present paper, we aim to study the underbody flow of the train with two bogie cavity configurations and also to study their effects on the near wake structures, as well as the aerodynamic drag force. Here, to simulate a realistic wind tunnel environment, a stationary ground is used in the simulations. This is because most wind tunnels do not have moving belts or suction devices to remove the boundary layers on the ground. Remind that the organization of the paper is as follows: In Section 2 the numerical method is described. In Section 3 computational details for the numerical simulations and the

research question are depicted. In Section 4, relevant definitions of the non-dimensional coefficients are presented. Section 5 introduces the results from previous wind tunnel tests and compares these with the numerical data to validate the numerical method and mesh strategy. Subsequently, the underbody flow fields and near wake structures of the train are analysed. This is followed by Conclusions in Section 6.

2. NUMERICAL METHOD

CFD (computational fluid dynamics) researchers have been seeking a numerical method which can reduce the massive demands of computing resources in LES (large eddy simulation) where is away from the near-wall, but improve the accuracy of RANS (Reynolds-averaged Navier-Stokes) applied to the near-wall regions (Fluent Inc., 2011). DES (detached eddy simulation) is a representative hybrid RANS–LES method that was originally proposed by Spalart *et al.* (1997). With fast development in turbulence model, the DES is becoming a promising method in modelling separated flows at high Reynolds numbers, showing a good prediction in the external flow around ground transport vehicles (Favre and Efraimsson, 2011; Guilmineau *et al.,* 2013; Flynn *et al.,* 2014; Morden *et al.,* 2015; Huang *et al.,* 2016; Niu *et al.,* 2017; Zhu *et al.,* 2017; Zhang *et al.,* 2016, 2017 and 2018a).

In the present study, the RANS model, Realizable k-ε, was employed to the near-wall regions. It has been used in previous work for trains (Zhang *et al.,* 2016 and 2018a) provides superior performance for flows involving rotation, boundary layers with adverse pressure gradients, separation and recirculation (Fluent Inc., 2011)

3. COMPUTATIONAL DETAILS

A simplified 1/8th-scale high-speed train model is shown in Fig. 1. This reduced-model was constructed according to the experimental model from wind tunnel tests (Zhang and Zhou, 2013); the head, middle and tail cars are grouped together to form a train-set with bogies and inter-carriage gaps, see Fig. 1. The total length L of the train was 9.55 m, with train height H of 0.4625 m and width W of 0.4225 m. In the wind tunnel tests, to measure the drag forces on each car, separately, a small gap is implemented between two neighbouring coaches. This is also the case in the numerical simulations.

Figure 2 shows the outlines of train models with two different bogie cavity configurations in the symmetry plane. The straight ends in the regions of the train model is specified as Case 1 which is actually the same as the one used in the wind tunnel tests, Fig. 2(a). In Fig. 2(b), both front and rear surfaces were slanted at an angle of $\cot\beta = 0.5$, defined as Case 2. Note that the front end of the first bogie region and the rear end of the last bogie region were always made vertical to save space.
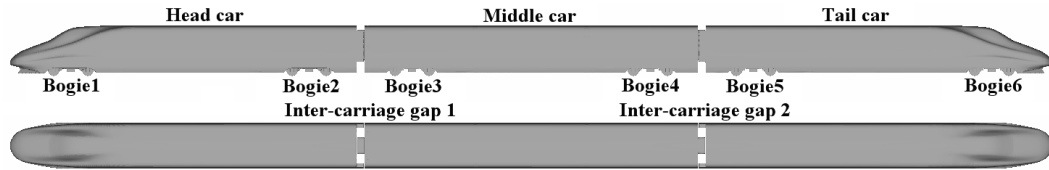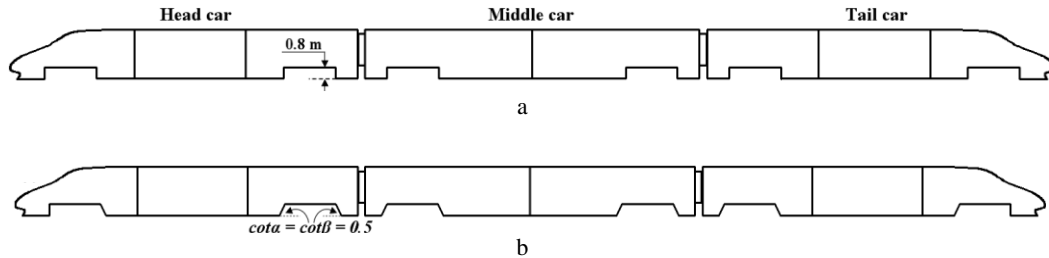
Fig. 1. High-speed train model.

Fig. 2. Different bogie cavity configurations: (a) Case 1, (b) Case 2.
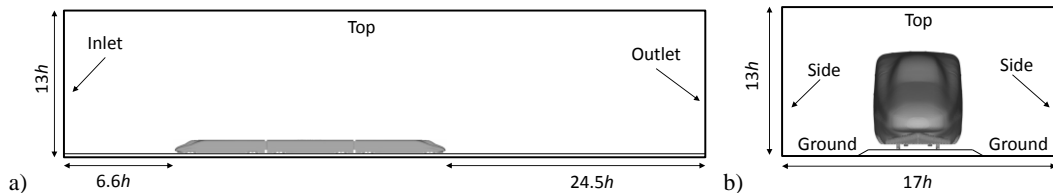

Fig. 3. Computational zone: (a) Side view; (b) Front view.

Fig. 4. Computational mesh.

The train model shown in Fig. 1 is mounted in a closed computational domain with a blockage of 0.443% (see Fig. 3). To simulate the train speed, a uniform velocity profile was applied at the inlet, leading to a Reynolds number of 1.8×10^6 based on the inlet velocity U_{inf} and the train height H. As to the outlet boundary condition, static pressure of zero was assigned. The top and sides were all set as symmetry. Here, considered a realistic wind tunnel environment, the stationary ground was used in simulations, since most wind tunnels do not have moving belts or suction devices to remove the boundary layers on the ground.

In this paper, a hexahedral dominated mesh around the high-speed train is generated using an open-source CFD toolbox, OpenFOAM (Open Source Field Operation and Manipulation) (OpenFOAM, 2014). Its pre-processing package SnappyHexMesh provides an efficient and fast method to build the mesh automatically and allows most of cells to

locate in the regions close to the train body. Due to those advantages, this grid generation strategy has been widely used in simulating the external flow fields around trains (Flynn *et al.,* 2014; Zhang *et al.,* 2016, 2017 and 2018a; Niu *et al.,* 2017; Morden *et al.,* 2015). Before determined which grid is suitable for the simulations, a grid-independence test should be conducted in the beginning. However, in this study, when the medium mesh was used, less than 2% difference is found in drag forces as compared to the coarse mesh, Table 1. Therefore, to save computing resources, we stopped the test and believed that the medium mesh is sufficient to be used. Figure 4 shows the mesh distribution on/around the train in the medium mesh. To ensure high-level grid resolution in the near region of the train, a refinement boxes is placed on the ground, with the dimensions of $35H \times 2.5H \times 1.35H$, as shown in Fig. 4. The smallest size of the train surface mesh is 2.0 mm; with the thickness of the first layer being 0.2 mm to ensure the y+

Table 1 C_d of each car in the present numerical simulations and previous wind tunnel tests

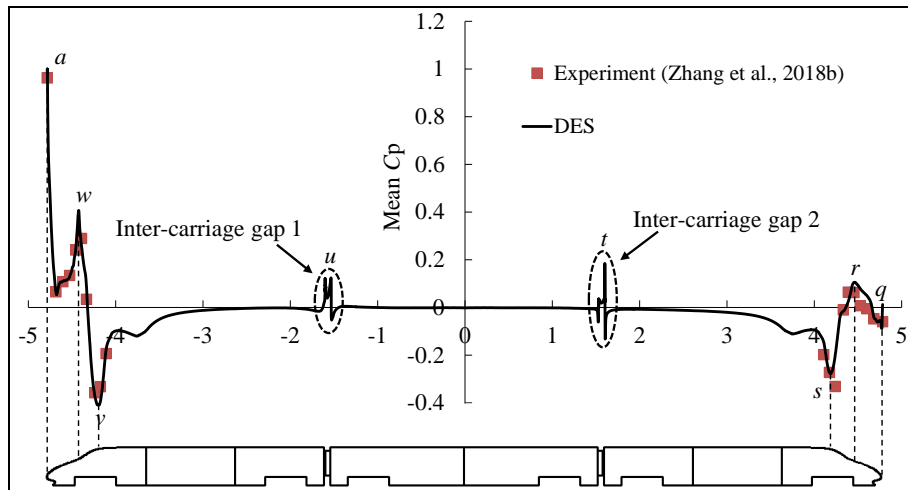| Method	Grid	Cells	$C_{d\text{-Head car}}$	$C_{d\text{-Middle car}}$	$C_{d\text{-Tail car}}$
Numerical simulation	Coarse grid	20 million	0.149	0.077	0.159
	Medium grid	28 million	0.147	0.080	0.160
Wind tunnel test (Zhang and Zhou, 2013)	-	-	0.145	-	0.163

Fig. 5. Time-averaged pressure distribution along the symmetric upper profile of the train in the present numerical simulations and wind tunnel tests (Zhang *et al.,* 2018b).
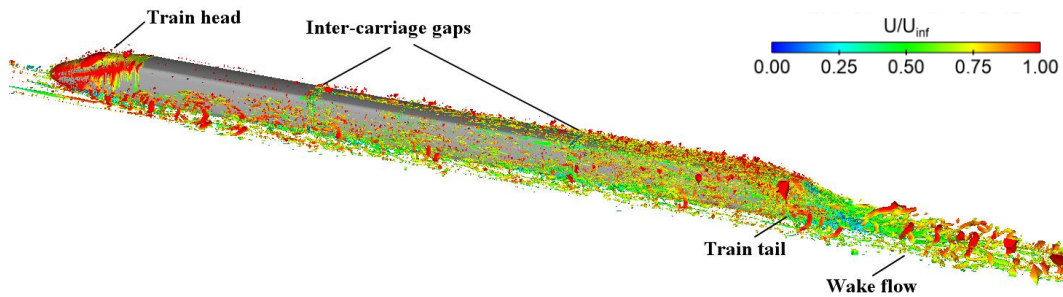

Fig. 6. Instantaneous vortex structures around the high-speed train - iso-surface plot of Q=50000. Flow comes from top left to bottom right.

requirements in using wall function of turbulence models (30 < y+ < 300). Note that 10 prism layers in a belt around the train body were used to capture the near-wall flow features.

To solve this typical underbody and near wake flow of the train, a pressure-based solver in Fluent was adopted for the simulations. The Finite Volume Method (FVM) based on cell centres was adopted for the discretization of the controlling equations, while the SIMPLE (Semi-Implicit Method for Pressure-Linked Equations) algorithm was used to couple the pressure and velocity fields. For the convective terms a bounded central differencing scheme was assigned; for the dissipative terms the second-order upwind scheme was utilised. In addition, for this unsteady flow simulation the second-order implicit scheme was always applied to solve the time derivative. The residual value of continuity equation was set at 10^{-4} to guarantee the flow converged. Also to ensure the flow fully developed, the aerodynamic force coefficients of cars are monitored to check every flow passage.

The physical time step, usually normalised by the incoming flow velocity U_{inf} and train height H, is $\Delta t = 0.0065$, keeping a CFL number around 1.0 all over the domain. In all cases, the initial flow passage was used to make the flow fully developed; after that, the variables were averaged over two passages through the domain.

4. RELEVANT DEFINITIONS

To conveniently make a comparison of different

train models, the aerodynamic drag, static pressure on the train body and time are normalised as follows (CEN, 2010 and 2013).

$$C_d = F_d / (0.5U_{\text{inf}}^2 S) \qquad (1)$$

$$C_p = (p - p_{ref}) / (0.5U_{\text{inf}}^2 S) \qquad (2)$$

$$C_t = tU_{\text{inf}} / H \qquad (3)$$

Where, F_d is the aerodynamic drag; C_d is the aerodynamic drag coefficient; C_p is the static pressure coefficient; C_t is the non-dimensional time. ρ is the constant air density (taken as 1.225 kg/m³). U_{inf} is the incoming flow speed, p is the static pressure on the train surface, p_{ref} is the reference pressure (taken as 0). S is the reference area (taken as the frontal area, which is 0.175 m² here). t is the computation time in the simulation.

5. RESULTS AND DISCUSSION

5.1 Program Validation

A wind tunnel test on the aerodynamic drag of the high-speed train has been carried out in the Low Speed Aerodynamic Institute of China Aerodynamics Research & Development Center (CARDC). The detail information about the wind tunnel test can be found from Zhang and Zhou (2013) and Zhang *et al.* (2018b). To validate the resolution of the mesh and the methodology used in this paper, the same geometry, blockage ratio, and inlet conditions were simulated in the verified case. Table 1 shows the validation results against previous wind tunnel tests (Zhang and Zhou, 2013). The general observation is that the drag coefficients C_d calculated in the simulations show good agreement with those from the wind tunnel tests. Therefore, it can be concluded that the simulations with the resolution of the mesh and the methodology in this study can predict highly accurate flow behaviours of the train. Furthermore, Fig. 5 shows the comparison of time-averaged pressure coefficients along the symmetric upper profile of the train obtained by DES on the medium mesh and a previous wind tunnel test. Although a few measurement points show larger differences, the simulation results are consistent with the experimental data.

5.2 Underbody flow Structures

The second invariant Q with a positive value that is first proposed by Hunt *et al.* (1988) is widely used to describe the instantaneous flow structure, presenting where the vortices are. Figure 6 shows the instantaneous vortices using iso-surface plot of Q=50000 in Case 1, coloured with velocity magnitude.

Clearly, the train is surrounded by massive vortices, in particular for the head, inter-carriage gaps, bogie regions and the near wake, similar to what has been found in Huang *et al.* (2016), Zhang *et al.* (2016 and 2018a) and Niu *et al.* (2017). There are fewer vortices around the upper body of the train as compared to the lower regions close to the ballast and ground, where the complex geometry of the bogies generates strong vortices that rapidly become chaotic, leading to regions of high turbulence at the bottom of the train. In the wake, massive separation shedding from the streamlined head of the tail car, contributing to a large number of low velocity vortices, as well as large fluctuations, as shown in Fig. 6.

It is difficult to find out the differences in the cases through the instantaneous flow structure as shown in Fig. 6, due to the chaotic vortices around the train, especially underneath the train bottom. Thus, a middle plane along the train length with mean velocity vector is set up to explore the flow structures in the cases. Some differences can be clearly found in Fig. 7. For example, in the bogie 1 region, in the front the vector contour seems to be similar due to the same angle of the plate, actually the velocity profiles presented in Fig. 8(b) are almost the same within the identical ground condition; in the rear the velocity changes a lot with a large vortex being formed and flow direction reversing, achieving lower velocities in Case 1 (with straight plates in the bogie cavities), as shown in Fig. 8. In other bogie regions it is also very easy to distinguish the differences in the two cases, especially for the vortices and velocity magnitudes. For the inclined plate in the front the velocity is lower below the height of the train bottom, Fig. 8(b). However, it is a little higher in the bogie region where is enough space for the flow to raise an angle, which can impact on the bogie structure in the rear leading to positive pressure and drag increase.

Figure 8 shows the comparison of time-averaged streamwise velocity profiles underneath the train bottom along eight specified lines from the first bogie cavity to the last one in the vertical midplane. The general observation is that the velocity in the gap decreases along the flow direction. With regards to a certain line, the velocity profiles in both cases present the same trend below the height of the train bottom; an increase to the maximum, then with a decrease. However, above this height, the angle effect of the bogie cavities becomes the dominant role in these regions. The Case 1, with straight plates at the ends of the bogie cavity, shows faster changes of the velocity profiles at each location (see Fig. 8(b)). In the rear of each bogie region, the plate angle and inter-carriage gaps contribute too much to the velocity profiles, as shown in Fig. 8(b).

In Fig. 9, the time-averaged streamwise velocity u and static pressure C_p profiles underneath the train in the two cases are used to deeply explore the flow characteristics below the bottom. Figure 9(a) shows the specific location of the lines. Here, lines l_1 and l_2 lie in the vertical midplane, of which line l_1 locates at the top of the rail, while l_2 is in the middle of the clearance from the train bottom to the rail top. Overall, the complex configurations of the bogie cavities cause the gradient change of the
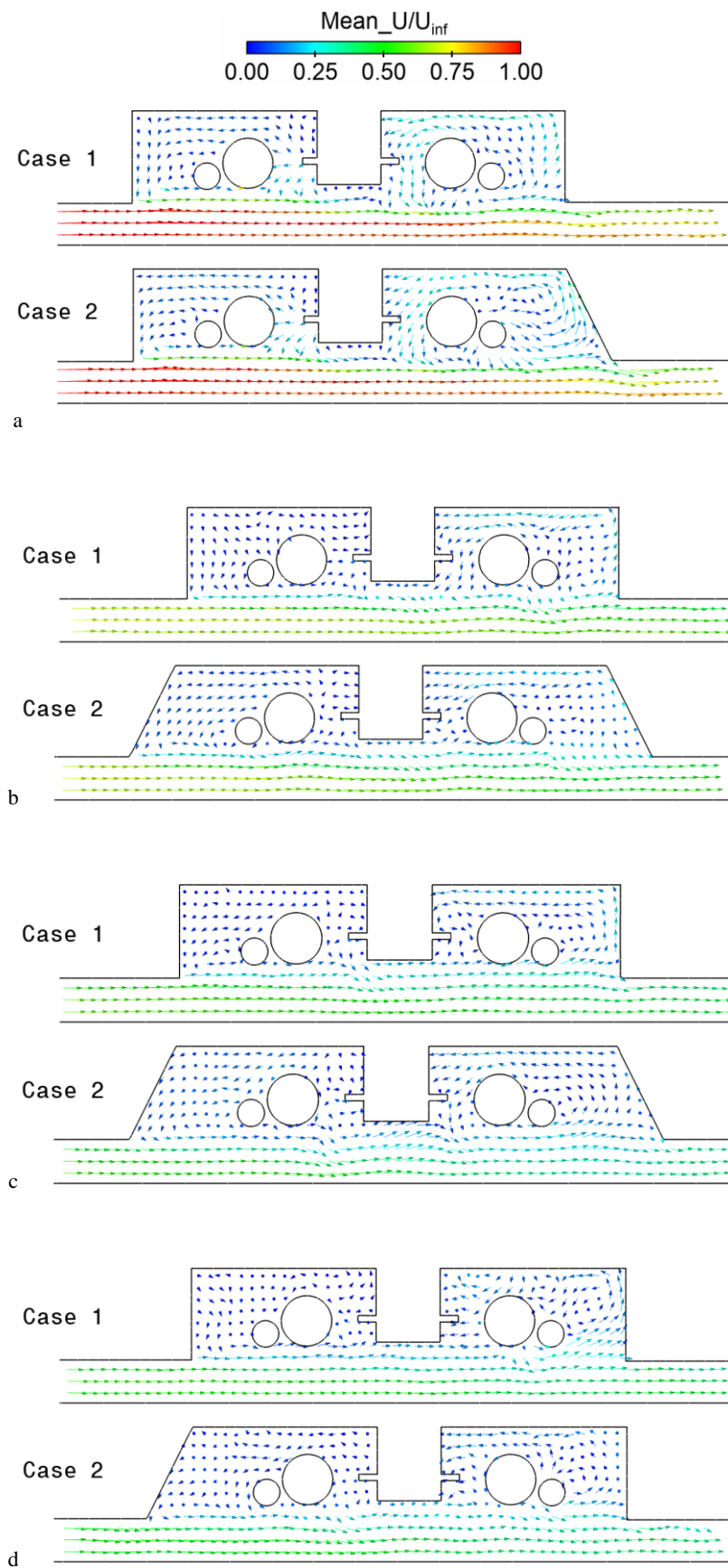
Fig. 7. Velocity vector in different bogie regions at Y=0: (a) Bogie 1 region, (b) Bogie 2 region, (c) Bogie 3 region, (d) Bogie 6 region.
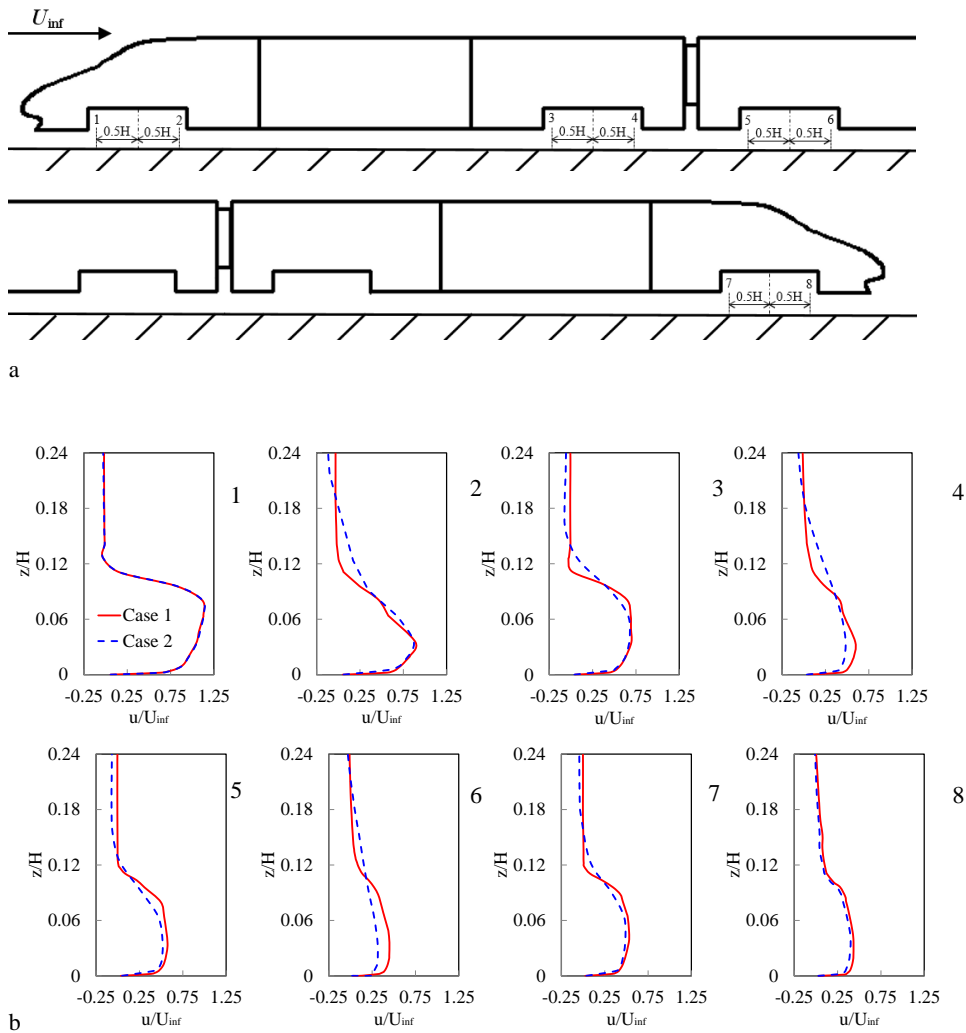
Fig. 8. Comparison of time-averaged streamwise velocity *u* underneath the train bottom along eight specified lines in the vertical midplane: (a) Location of profiles. (b) *u* profiles.

velocity and pressure around the region, i.e. the fluctuations underneath the train. Eight peak-to-peak changes of velocity and pressure profiles can be seen in those figures, respectively, due to the streamlined head/tail and six bogie cavities. Larger differences of velocity profiles for the two cases are observed, starting from the rear of the bogie 1 region until the near wake, particularly underneath the middle coach. The Case 1 gives a little higher velocity and larger fluctuation than the Case 2 within the stationary ground boundary condition. In the bogie regions, the angles of the plates play a dominant role in the velocity fluctuation. Furthermore, the C_p profiles of the two cases at different height show the same trends.

5.3 Pressure Distributions on Train Bottom

The previous studies (Zhang *et al.,* 2016 and 2018a; Niu *et al.,* 2017) have shown that the bottom configuration has little effect on the upper surface pressure of the train, so only the pressure profiles

on the train bottom in the vertical midplane are analysed, as shown in Fig. 10.

In Fig. 10 the point *a* is a stagnation point with the largest positive pressure coefficient. A second peak in pressure is found at point *b*, this being due to the structure of head nose. This is a double peak with a positive peak value and a negative peak value. At point *c*, the angles of the bogie cavities for two cases are very similar with a step change in pressure. Following this, a difference is found at point *d*. Note that in Case 1 the peak-peak value is larger. This is because the vertical end in the rear of Case 1 enhance the change of the velocity gradient as compared to the more gradual transition in Case 2. As to the amplitude, the positive peak is also larger in Case 1, but the absolute value of the negative is less. Following this the C_p increases slowly along the head car body until it stabilizes at a slightly positive value. In the bogie 2 region the C_p is positive and the pressures for cases are very similar in magnitude and form. From point *f* to point *h*, due to the inter-carriage gap covered by a
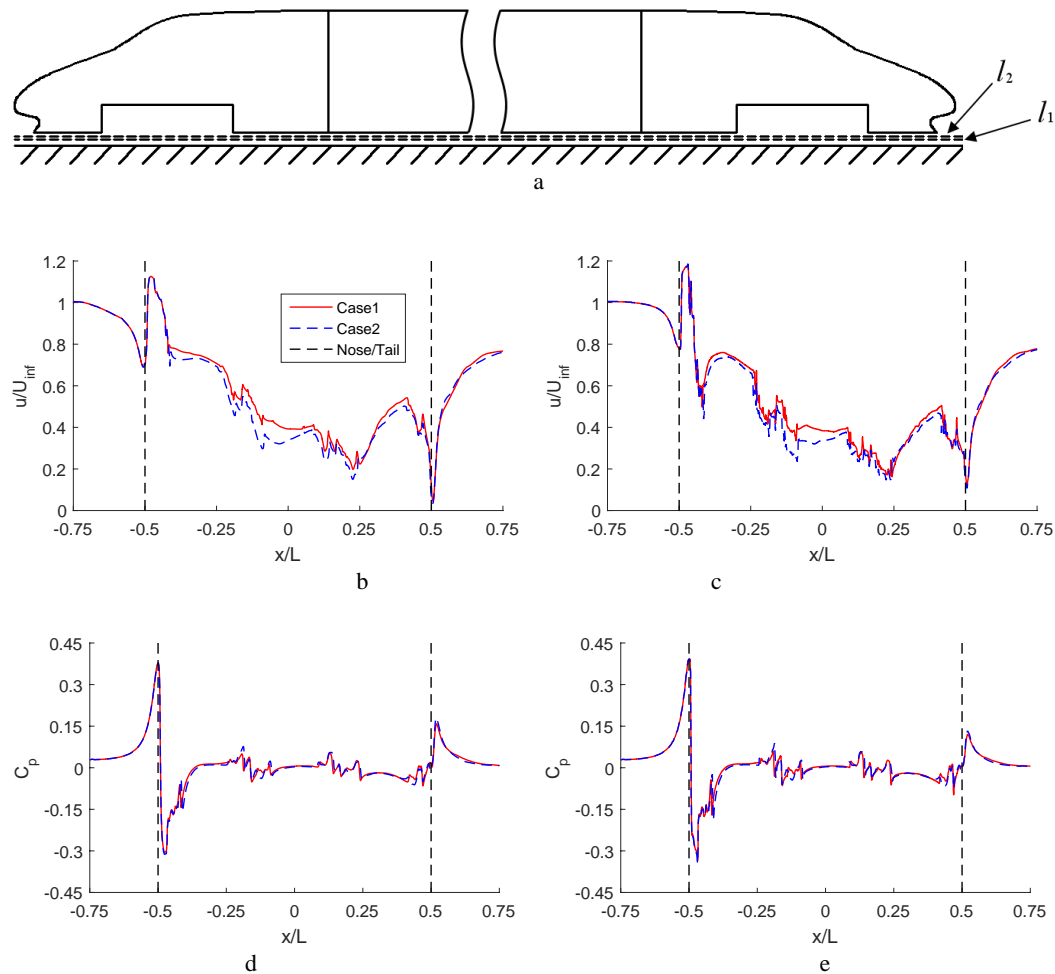
Fig. 9. *u* and C_p distributions along two lines underneath the train bottom in the vertical midplane: (a) Profiles' location. (b) *u* profiles along l_1. (c) *u* profiles along l_2. (d) C_p profiles along l_1. (e) C_p profiles along l_2.

semi-closed windshield, there are some pressure fluctuations. At the bogie 3 region, although the variation is similar to that in the bogie 2 region, the geometries with the vertical end cause an increment in the pressure magnitude at point *i*. Along the middle car body, there is a slightly positive or negative pressure over the surface. The variation of C_p from point *j* to point *n* can be seen to be similar to that from point *e* to point *i*, but the pressure magnitude is slightly less. Along the tail car body, a slightly negative pressure is generated on the car's surface. From point *o* to point *p*, due to the inclined front end in the cavity, Case 2 shows a smaller pressure.

Based on the above analysis, the difference of pressure distribution only appears at the bogie regions. Thus, more detailed information of the mean C_p on the bottom of the train and the bogies are depicted in Fig. 11 in order to understand how the bogie cavities affect the train surface pressure distribution.

In each bogie region, small positive or negative pressure appears at the front end. Due to the blockage by the under-body from the bogie cavities,

the positive pressure comes up in the rear of the bogie region, especially on the end plate. Also, the windward side of each bogie is impacted by the air, resulting in the positive pressure. In the bogie 1 region, the negative pressure is clearly dominant. In contrast, in the bogie 2 region, mostly there is positive pressure. However, there is little difference in the cases. Along the length of the head car, it can be clearly discovered that the pressure increases from bogie 1 to bogie 2. In the bogie 3 region, the front inclined bogie cavity mitigates the pressure, but the end vertical cover causes a pressure increase. Overall, most part of the region suffers a small negative pressure. To the authors' knowledge, the pressure distributions on the bogie 4 and bogie 5 regions show slight differences from those on the bogie 2 and bogie 3 regions, respectively, so they will not be analysed and discussed in the following section. In the bogie 6 area, the rear ends keep straight in both cases; as discussed in Fig. 10, the front inclined end mitigate the pressure change.

In both cases, when the flow underneath the train travels from the head to the wake, it runs into the bogie cavity and rise up, which causes that the
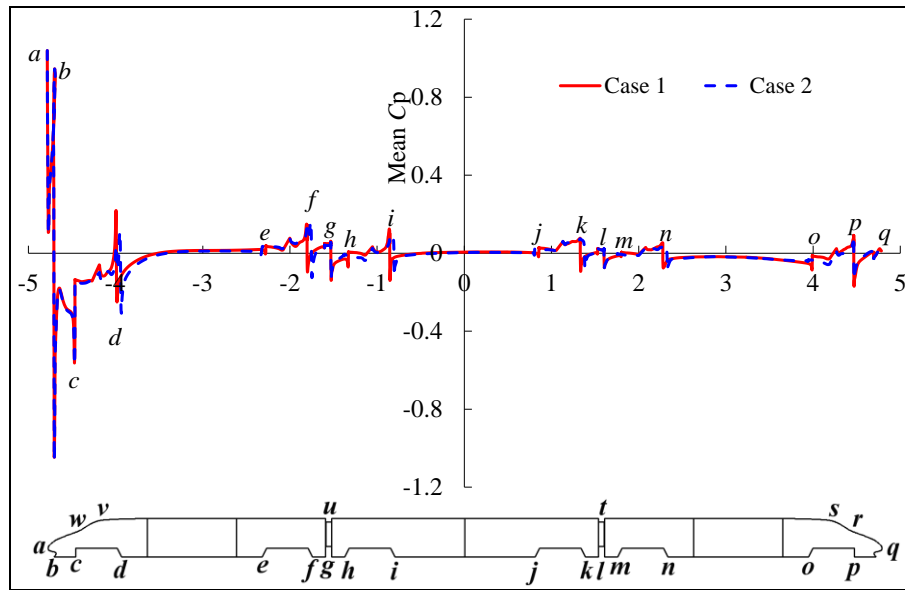
Fig. 10. C_p profiles along the train bottom in the vertical midplane.
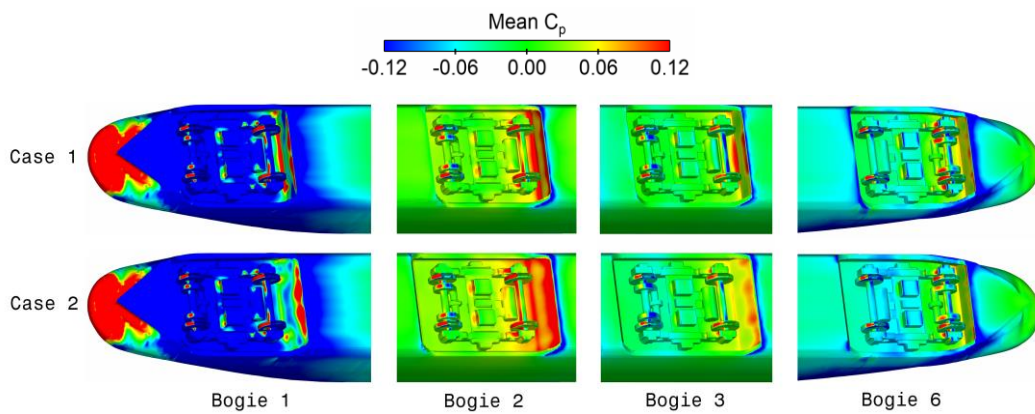

Fig. 11. Mean C_p on the bottom and the bogie regions of the train.

pressure on the second wheelset is higher. Due to the expansion in area of the cross-section, it now travels through, the flow angle increases and this acts on the end bogie cavity, which contributes to a flow being deflected and the air velocity decreasing. This occurs irrespective of whether there is a vertical face or an inclined one. As a result, the pressure on the surrounding surface increases.

5.4 Near Wake Structures

Figure 12 shows the time-averaged streamwise velocity contours in the lateral plane (z=0.12125H) and symmetry plane (y=0H) in the near wake of the two cases. Note that the distinguished differences are observed. As the stationary ground is used for the two cases, in Case 2 inclined ends lead to more energy dissipation in the bogie region, resulting in low velocity, as well as a longer pair of low velocity regions in the wake as compared to Case 1 (see Figs. 12(a) and (c)). In the symmetry plane, two large vertices are shown below the nose and

adjacent to the ballast in Figs. 12(b) and (d), respectively. One, defined as V1, is close to the nose tip, and the other, specified as V2, is attached on the ballast, which is similar to the flow structures behind a square back of the ground transportation vehicle model (Rao *et al.,* 2018a and 2018b) but without seeing the stretched narrow vertex in the right top region. In Case 1, the centers of V1 and V2 are both a little far away from the obstacle deflector, and the velocity in the near wake is relatively higher as compared to Case 2.

5.5 Aerodynamic Drag Coefficients

Table 2 lists the time-averaged drag coefficients of each car and the entire train using the medium mesh. Generally, less air impacting on the ends of the bogie cavity leads to a smaller drag force on the car/train. Therefore, Case 2 with inclined plates of the bogie cavities shows larger forces. Note that in both cases the aerodynamic drag of the head car is less as compared to the tail car. Considered the total
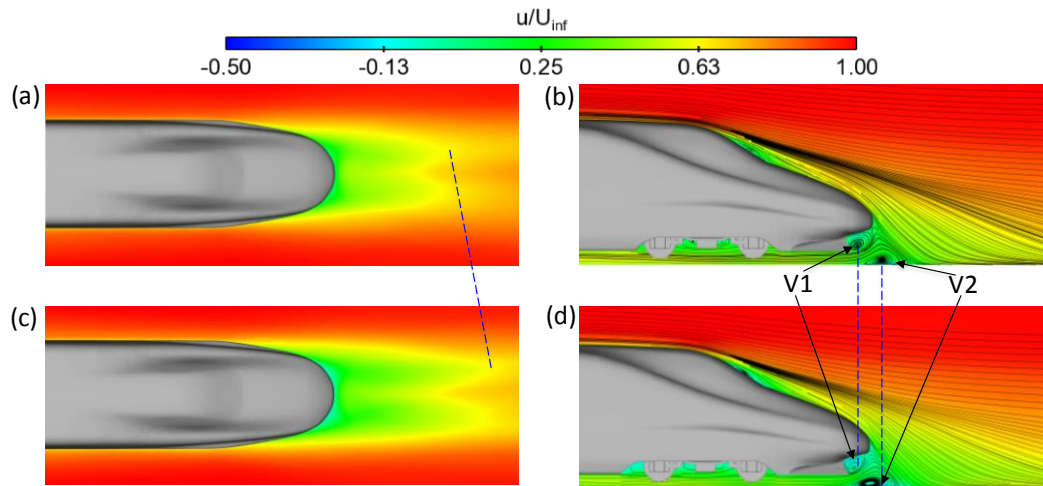
Fig. 12. Near wake structures for two cases: (a) time-averaged streamwise velocity contours at z=0.12125*H* and (b) time-averaged streamwise velocity contours overlaid with streamlines at y=0*H* for Case 1; (c) time-averaged streamwise velocity contours at z=0.12125*H* and (d) time-averaged streamwise velocity contours overlaid with streamlines at y=0*H* for Case 2.

drag, Case 2 increases by 2.8%. Therefore, when thinking about how to simplify the bogie cavity of the train model, it should be more realistic.

Table 2 Aerodynamic drag coefficient C_d of each part

Car	C_d	
	Case 1	Case 2
Head car	0.147	0.157
Middle car	0.080	0.083
Tail car	0.160	0.158
Total	0.387	0.398

6. CONCLUSIONS

Hybrid RANS–LES methods such as DES can accurately capture the instantaneous and time-averaged information at a lower computational cost but with the accuracy of LES. In this paper, the approach with the Realizable k-ε turbulence model applied to the near-wall region was used to study the effects of bogie cavity configurations on the underbody flow and near wake structures of the high-speed train at the Reynolds number of 1.8×10^6. The mesh strategy and methodology were validated against the previous wind tunnel tests, showing good agreement. The instantaneous and time-averaged flow structures underneath the train and in the near wake, the mean pressure on the train bottom and the aerodynamic drag coefficients for both cases were investigated. The results show that highly complex flow vortices appear around the bogie regions. The pressure distributions on the train bottom are basically the same, except of the bogie regions. When the straight walls are used in the bogie regions, the whole train experiences a lower drag force. Thus, in order to obtain more accurate force coefficients, a precise simplification

criterion should be taken into account, although this small configuration only leads to about 3% deviation.

REFERENCES

CEN European Standard (2010). *Railway applications– aerodynamics*. Part 6: requirements and test procedures for cross wind assessment, CEN EN 14067-6.

CEN European Standard (2013). *Railway applications– aerodynamics*. Part 4: requirements and test procedures for aerodynamics on open track, CEN EN 14067-4.

Favre, T. and G. Efraimsson (2011). An assessment of detached-eddy simulations of unsteady crosswind aerodynamics of road vehicles. *Flow, Turbulence and Combustion* 87(1), 132−163.

Fluent Inc. FLUENT User's Guide (2011).

Flynn, D., H. Hemida, D. Soper and C. Baker (2014). Detached-eddy simulation of the slipstream of an operational freight train.

Journal of Wind Engineering and Industrial Aerodynamics 132, 1-12.

Gao, G. J., F. Li, K. He, J. B. Wang, J. Zhang and X. J. Miao (2018). Investigation of bogie positions on the aerodynamic drag and near wake structure of a high-speed train. *Journal of Wind Engineering and Industrial Aerodynamics, in press.*

Guilmineau, E., O. Chikhaoui, G. B. Deng and M. Visonneau (2013). Cross wind effects on a simplified car model by a DES approach. *Computers & Fluids* 78, 29-40.

Huang, S., H. Hemida and M. Z. Yang (2016). Numerical calculation of the slipstream generated by a CRH2 high-speed train. *Proc. Inst. Mech. Eng. - Part F J. Rail Rapid Transit* 230 (1), 103–116.

Hunt, J. C. R., A. A. Wray and P. Moin (1988). Eddies, streams, and convergence zones in turbulent flows. *In: Studying Turbulence Using Numerical Simulation Databases, 2: Proceedings of the Summer Program* 193–207.

Mancini, G., A. Malfatti, A. G. Violi and G. Matschke (2001). Effects of experimental bogie fairings on the aerodynamic drag of the ETR 500 high speed train. *Proceedings of the World Congress on Railway Research*, 25-29 November, Koln, Germany.

Morden, J. A., H. Hemida and C. J. Baker (2015). Comparison of RANS and detached eddy simulation results to wind- tunnel data for the surface pressures upon a class 43 highspeed train. *Journal of Fluids Engineering* 137, 41108–41109.

Niu, J. Q., D. Zhou and X. F. Liang (2017). Numerical simulation of the effects of obstacle deflectors on the aerodynamic performance of stationary high-speed trains at two yaw angles. *Proceedings of the Institution of Mechanical Engineers, Part F: Journal of Rail and Rapid Transit, 232.*

Openfoam (2014). OpenCFD, http://www. openfoam.com/.

Rao, A. N., G. Minelli, J. Zhang, B. Basara and S. Krajnović (2018b). Investigation of the near-wake flow topology of a simplified heavy vehicle using PANS simulations. *Journal of Wind Engineering and Industrial Aerodynamics* 183, 243-272.

Rao, A. N., J. Zhang, G. Minelli, B. Basara and S.

Krajnović (2018a). An LES Investigation of the Near-Wake Flow Topology of a Simplified Heavy Vehicle, Flow. *Turbulence and Combustion.*

Spalart, P. R., W. H. Jou, M. Strelets and S. R. Allmaras (1997). Comments on the feas1ibility of LES for wings, and on a hybrid RANS/LES approach. *Proceedings of first AFOSR international conference on DNS/LES*, Ruston, Louisiana. Greyden Press, 4–8 Aug.

Zhang, J., J. B. Wang, Q. X. Wang, X. H. Xiong G. J. Gao (2018a). A study of the influence of bogie cut outs' angles on the aerodynamic performance of a high-speed train. *Journal of Wind Engineering and Industrial Aerodynamics* 175, 153-168.

Zhang, J., J. J. Li, H. Q. Tian, G. J. Gao and J. Sheridan (2016). Impact of ground and wheel boundary conditions on numerical simulation of the high-speed train aerodynamic performance. *Journal of Fluids and Structures* 61, 249-261.

Zhang, J., K. He, X. Xiong, J. Wang and G. Gao (2017). Numerical simulation with a DES approach for a high-speed train subjected to the crosswind. *Journal of Applied Fluid Mechanics* 10 (5), 1329–1342.

Zhang, L., M. Z. Yang, X. F. Liang (2018b). Experimental study on the effect of wind angles on pressure distribution of train streamlined zone and train aerodynamic forces. *Journal of Wind Engineering & Industrial Aerodynamics* 174, 330-343.

Zhang, Z. Z. and D. Zhou (2013). Wind tunnel experiment on aerodynamic characteristic of streamline head of high speed train with different head shapes. *Journal of Central South University* (Science and Technology) 44(6), 2603-2608.

Zheng, X. H., J. Y. Zhang and W. H. Zhang (2011). Numerical simulation of aerodynamic drag for high speed train bogie. *Journal of Traffic and Transportation Engineering* 11(2), 45-51.

Zhu C. L., H. Hemida, D. Flynn, C. Baker, X. F. Liang and D. Zhou (2017). Numerical simulation of the slipstream and aeroacoustic field around a high-speed train. *Proceedings of the Institution of Mechanical Engineers, Part F: Journal of Rail and Rapid Transit* 231(6), 740-756.